

Quantitatively Characterized Crystallization Effect on Recombination Energy Loss in Non-Fullerene Organic Solar Cells

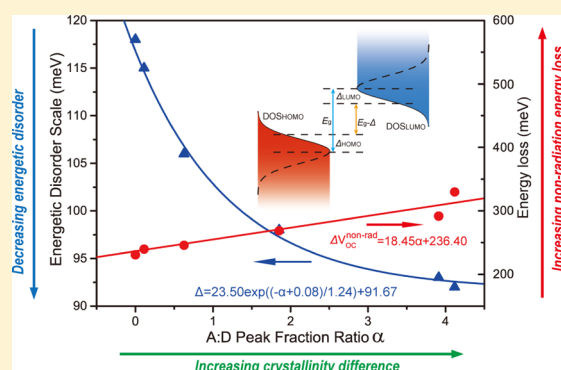
Zhi-Hao Chen,[†] Peng-Qing Bi,[†] Xiao-Yu Yang,[†] Meng-Si Niu,[†] Kang-Ning Zhang,[†] Lin Feng,[†] and Xiao-Tao Hao^{*,†,‡}

[†]School of Physics, State Key Laboratory of Crystal Materials, Shandong University, Jinan, Shandong 250100, China

[‡]ARC Centre of Excellence in Exciton Science, School of Chemistry, The University of Melbourne, Parkville, Victoria 3010, Australia

Supporting Information

ABSTRACT: Recombination energy loss is the main impediment on improving the power conversion efficiency of organic solar cells (OSCs). The pernicious effect is usually induced by two dynamics, that is, the geminate recombination of nascent charge pairs soon after the exciton dissociation and nongeminate recombination of separated charges during their transportation. Both hinder achieving high open-circuit voltage (V_{OC}). Here, we comprehensively investigated the relationship between crystallization and molecular recombination in a non-fullerene system of poly[(2,6-(4,8-bis(5-(2-ethylhexyl)thiophen-2-yl)benzo[1,2-*b*:4,5-*b'*]dithiophene)-*co*-(1,3-di(5-thiophene-2-yl)-5,7-bis(2-ethylhexyl)-benzo[1,2-*c*:4,5-*c'*]dithiophene-4,8-dione))] (PBDB-T):((5Z,5OZ)-5,50-(((4,4,9,9-tetraoctyl-4,9-dihydro-s-indaceno[1,2-*b*:5,6-*b'*]dithiophene-2,7-diyl)bis(benzo[*c*][1,2,5-thiadiazole-7,4-diyl))bis(methanylylidene))bis(3-ethyl-2-thioxothiazolidin-4-one)) (O-IDTBR). Based on a quantitative characterization of crystallinity, it was found that the crystallization intensity ratio between components is the key factor to suppress recombination energy losses. The nongeminate recombination showed increased probability with enlarged variance of crystallinity between the donor and acceptor. The geminate recombination was proven to be restricted by the energetic disorder of the highest occupied molecular orbital and lowest unoccupied molecular orbital, as well as the phase separation induced by crystallization. The rational crystallization intensity ratio between donor/acceptor (D/A) components is vital in achieving minimum energy loss as well as best device performance. The results are favorable for comprehending the effects of crystallinity in charge transfer and charge transport dynamics and provide guidance for morphology and crystallinity optimization in non-fullerene OSCs.



1. INTRODUCTION

With the advantages of the broadened solar light absorption region, improved charge transport property, and tunable energy levels, organic bulk heterojunctions (BHJ) based on non-fullerene molecules have become the cutting edge of organic solar cells (OSCs) design and fabrication, stimulating the power conversion efficiency (PCEs) in single-junction OSCs to exceed 15% as reported recently.¹ The relative large band gap of non-fullerene materials is the foundation of high V_{OC} .^{2–5} With the rapid progress in the material synthesis, non-fullerene material-based OSCs have encouraged V_{OC} beyond 1.0 V which enable the OSC achieving high PCE.^{6–10} However, comparing with the energetics difference between the highest occupied molecular orbital (HOMO) of the donor and the lowest unoccupied molecular orbital (LUMO) of the acceptor, the energy losses, especially losses in V_{OC} , still exhibit a relative large scale which impedes further improvements in device performance.

Previous studies show that V_{OC} has a close relationship with the energy of charge transfer states (CTS), E_{CT} , at the D/A

interfacial area which theoretically sets the upper limit of V_{OC} .^{11,12} The difference between E_{CT} and V_{OC} mainly originated from the nongeminate recombination, which contains radiative and nonradiative pathways, generally found to be around 0.6 V.^{13–15} The radiative loss is an intrinsic property originating from the blackbody theory and unrealistic to be adjusted. The nonradiative part, although proven to be unavoidable due to the electron–phonon coupling,¹⁶ could be manipulated during film fabrication through controlling the morphology and crystallization. Geminate recombination is another loss channel that needs to be taken in account. Energetics of D/A materials have close relationship with the geminate recombination mechanism. In recent few years, it has been accepted that the energetic structure in solid films of conjugated materials is far more complex than the oversimplified single-energy levels. Inhomogeneous broadening of density of states (DOSs), that is energetic disorder, has been

Received: April 16, 2019

Published: April 30, 2019

proved to be a crucial factor affecting V_{OC} .^{17,18} The scale of energetic disorder can be manipulated through many aspects. Recently, Yang et al. applied solvent vapor annealing to improve the crystallinity of the donor and the acceptor in non-fullerene OSCs and achieved minimal nonradiative recombination energy loss.¹⁹ Wang and co-workers revealed the suppression of bimolecular recombination enabled by augmented effective internal electric field in non-fullerene OSCs.²⁰ Xie et al. compared the energetic disorder in fullerene- and non-fullerene-based OSCs, indicating that BHJ films containing non-fullerene materials have relative limited disorder scales induced by enhanced domain purity.²¹ Gao et al. reported that additive diiodooctane can enhance aggregation and phase separation of components, which is favorable for decreasing energetic disorder in the PBDTTT-C-T:PC₇₁BM blend.²² McGehee and co-workers pointed out that the crystalline polymer donors are capable of suppressing energetic disorder in fullerene-based OSCs, leading to a reduction of V_{OC} losses during burn-in.²³ Although endeavors have been concentrated on the connections between crystallinity and V_{OC} , quantified characterization is merely reported on the molecular crystallization behavior, leading a still blurry image of the intervening dynamics.

In this work, we comprehensively investigated the relationship between crystallinity variance of components and recombination mechanisms in OSCs based on poly[(2,6-(4,8-bis(5-(2-ethylhexyl)thiophen-2-yl)benzo[1,2-*b*:4,5-*b'*]-dithiophene)-*co*-(1,3-di(5-thiophene-2-yl)-5,7-bis(2-ethylhexyl)-benzo[1,2-*c*:4,5-*c'*]-dithiophene-4,8-dione))] (PBDB-T) and a high crystallinity non-fullerene acceptor ((5Z,5OZ)-5,50-(((4,4,9,9-tetraoctyl-4,9-dihydro-*s*-indaceno[1,2-*b*:5,6-*b*0]dithiophene-2,7-diyl)bis(benzo[*c*][1,2,5]thiadiazole-7,4-diyl))bis(methanylylidene))bis(3-ethyl-2-thioxothiazolidin-4-one)) (O-IDTBR). A quantified characterization of components crystallinity difference is illustrated based on grazing incidence wide-angle X-ray scattering (GIWAXS). Energetic disorders of corresponding states and exciton photoluminescence lifetimes are investigated to clarify gemination recombination. As a direct parameter, nonradiative recombination V_{OC} loss is calculated to estimate nongeminate recombination. This provides a quantitative perspective to understand the relationship between component crystallinity and energy loss dynamics and also guidance for photovoltaic performance optimization.

2. EXPERIMENTAL SECTION

PBDB-T was purchased from Solarmer, Inc. O-IDTBR was purchased from Derthon, Inc. All materials were used as received without further purification. OSCs were fabricated with the structure of ITO/PEDOT:PSS/PBDB-T:O-IDTBR/PFN-Br/Al. The hole transfer layer PEDOT:PSS (~30 nm) was deposited by spin-coating on ITO substrates at 5000 rpm and annealed at 150 °C for 20 min in air conditions. The BHJ solution was prepared in chlorobenzene with a D/A weight ratio of 1:1, totally 24 mg mL⁻¹. The BHJ films of 100 nm were solution-processed by spin-coating at 2500 rpm for 40 s. After that, the active layers were annealed at 80, 100, 120, 140, and 160 °C for 10 min in the nitrogen environment. The PFN-Br solution (0.5 mg mL⁻¹ in methyl alcohol) was spin-coated at 3000 rpm for 30 s to form a layer of ~5 nm thickness. Finally, the Al cathode (100 nm) was thermally evaporated on the PFN-Br at a pressure of 2.0×10^{-4} Pa. The active area of the device was 4 mm². Single-carrier devices have same active

layers while containing different electrodes and charge transfer layers with structures of ITO/ZnO/PBDB-T:O-IDTBR/Al for the hole-only device and ITO/PEDOT:PSS/PBDB-T:O-IDTBR/MoO₃/Ag. *J*-*V* characteristics for OSCs, and single-carrier devices were measured by a Keithley 2400 sourcemeter. For OSCs, the measurements were carried out under AM 1.5 G (100 mW cm⁻²) provided by an AAA solar simulator (Sofn Instruments Co., Ltd). External quantum efficiency (EQE) was measured using a 7-SCSpec system (Sofn Instruments Co., Ltd) under air conditions. For the temperature-correlated *J*-*V* characterization, the devices were sealed by the epoxy resin and then measured in a liquid nitrogen chamber, where temperature was adjusted by a temperature controller (TC280, East Changing, Inc.). The absorption spectra were obtained by a TU-1900 UV-vis dual beam spectrophotometer (PG Instruments, Ltd.). Reflectance spectra were measured by Agilent Cary 5000. The two-dimensional (2D) fluorescence lifetime images were acquired through a confocal optical microscope (Nanofinder FLEX2, Tokyo Instruments, Inc.) equipped with a time-correlated single-photon counting module (Becker & Hickl, SPC-150). Electroluminescence (EL) spectra were measured using the same confocal microscopy system, and bias was added by the Keithley 2400 sourcemeter, and EL signals were collected by an Edinburgh Instruments FLS980 spectrometer. Topography images were obtained using an atomic force microscope (AFM) in the tapping mode (Solver P47 PRO, NTMDT Co.). The GIWAXS experiment was performed at the beamline BL16B1 of Shanghai Synchrotron Radiation Facility. The wavelength and incidence angle of the X-ray beam are 0.124 nm and 0.08°, respectively, with a signal collecting detector 210 mm away from the sample.

3. RESULTS AND DISCUSSION

3.1. Material Properties. The chemical structures of the donor and the acceptor used in this work are shown in Figure 1a. Figure 1b shows the normalized absorption spectra of neat PBDB-T, neat O-IDTBR, and their blend films. The absorption spectrum of the PBDB-T film exhibits a plateau among 550–650 nm with two peaks located at 580 and 620 nm. The main absorption spectrum of neat O-IDTBR is in the range from 620 to 710 nm with a maximum at 685 nm, complementary to that of the donor. Both donor and acceptor films show relative high absorption intensity in the short wavelength region below 450 nm, which is beneficial to utilize the high energy photon. Figure 1c depicts the energy levels of PBDB-T and O-IDTBR. The HOMO level of PBDB-T is -5.33 eV, and the LUMO level of O-IDTBR is -3.80 eV.^{24,25} The difference of 1.53 eV between the HOMO of PBDB-T and the LUMO of O-IDTBR provides the potential of producing a high V_{OC} .

3.2. Quantitative Characterization of Crystallinity. To investigate the relationship between crystallization and recombination energy loss, it is crucial to acquire the crystallinity information of the BHJ films. Here, thermal annealing with different temperatures was applied to induce various crystallization of the donor and acceptor. AFM was used to examine the surface morphology of the pristine film without annealing (W/O) and blend films annealed at 80, 120, and 160 °C as shown in Figure S1. The pristine film exhibits a relative uniform distribution of D/A components with a smooth surface. In the film annealed at 80 °C, fiber-like structures and O-IDTBR crystalline grains appear among the

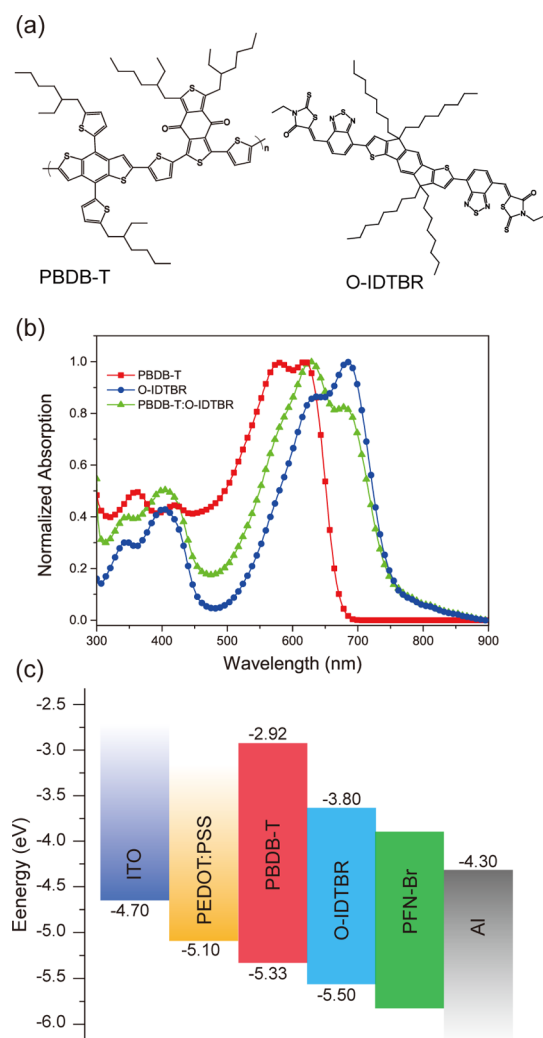


Figure 1. (a) Chemical structures of PBDB-T and O-IDTBR. (b) Normalized UV-vis absorption spectra of PBDB-T, O-IDTBR, and PBDB-T:O-IDTBR blend films. (c) Energy level diagrams of the materials used in OSCs.

films. With the annealing temperature rising, large grains appear in the active layer with 200–300 nm size along with flaws between crystal clusters, as shown in Figure S1c,d.

GIWAXS measurements were carried out to quantitatively investigate the crystallinity and molecular orientation of the BHJ films. The 2D GIWAXS patterns and corresponding in-plane (IP) and out-of-plane (OOP) direction intensity profiles of PBDB-T and O-IDTBR annealing-free neat films are shown in Figure S2. Well-ordered lamellar (100) and (300) peaks and strong π - π stacking (010) peaks in the OOP direction of the PBDB-T film indicate that the donor molecules are in high degree order.⁶ The (100) peak in the O-IDTBR film only appears in the IP direction with the (010) peak showing in OOP direction, implying O-IDTBR molecules prefer a face-on orientation. Figure 2 shows the 2D GIWAXS images and 1D profiles of annealed BHJ films. As the annealing temperature rises, 2D GIWAXS patterns exhibit intensive signals which confirm the enhanced degree of crystallization. For the OOP (010) peak representing π - π stacking, a superposition of multipeak components can be discovered in films with higher crystallinity (green and blue dash line in Figure 2g). Deconvolution of the subpeak contributions to the scanned

OOP (010) peaks reveals the crystallization property of the single donor and acceptor, and quantifies their individual contributions in each of the films. Peak fitting results of films annealed beyond 100 °C are illustrated in Figure S3 which shows that the broad peaks can be separated into three individual components: (010) peak of PBDB-T, (010) peak of O-IDTBR, and (020) peak of O-IDTBR. For the BHJ film annealed at 80 °C, O-IDTBR crystallinity is relative weak; thus, the original peak can only be fitted by 90.62% PBDB-T (010) fraction and 9.38% O-IDTBR (010) fraction, as shown in Figure S3a. For the film crystallized at 100 °C, the peak area fraction is 61.46, 29.06, and 9.48%, respectively. When temperature rises to 120 °C, the fraction rapidly increases to 46.52 and 18.46% for O-IDTBR (010) and (020) peaks, while the PBDB-T (010) peak only holds a part of 35.02%. In the conditions of 140 and 160 °C, the acceptor expands its fraction up to ~80% in which the part of the (010) peak is about 44% and the (020) peak is roughly 36% among the fitting area. This can be attributed to the stabilized crystallization intensities. These changes reveal that the acceptor molecules tend to crystallize more intensively compared with the polymer donor, thus leading to an initial decreasing and then increasing evolution of variance in D/A crystallinity. π - π stacking distances (d -spacing) and coherence lengths (CL) of PBDB-T and O-IDTBR (010) peak were estimated via $2\pi/q$ and $2\pi k/\Delta q$, respectively,²⁶ where q represents the peak position, k is a constant of 0.90, and Δq is the full width at half-maximum of the peak (summarized in Table S1). The d -spacings of both peaks are barely changed, showing the value around 0.36 and 0.33 nm of the donor and acceptor, respectively. However, O-IDTBR exhibits larger CL than PBDB-T under same annealing conditions, and the difference shows an enlarged tendency with the annealing temperature rising. The maximum CL value appears in 160 °C condition, in which CL is 7.89 and 4.07 nm for corresponding O-IDTBR and PBDB-T (010) peaks.

3.3. Photovoltaic Performance. To analyze recombination losses, it is necessary to acquire photovoltaic performance especially V_{OC} performance of corresponding crystallized BHJ films. Figure 3a shows current density versus voltage (J - V) curves of OSCs under AM 1.5 with active layers annealed at 80, 100, 120, 140, and 160 °C (insert schematic shows the device structure). Table 1 summarized the performance parameters of the devices. With more intensive crystallinity of the acceptor, V_{OC} exhibits an obvious dropping from 1.02 to 0.90 V, and short-circuit current (J_{SC}) values also show a shrinking trend reducing from 15.2 to 11.5 mA cm⁻². The reduction trends were illustrated in Figure 3d. The fill factor (FF) of OSCs without annealing exhibits a relative low value of 48.7%, while the value was increased to 55.0% with improved crystallinity. The highest PCE of 7.6% with a V_{OC} of 1.01 V, a J_{SC} of 14.2 mA cm⁻², and an FF of 53.1% was obtained among the OSC annealing at 80 °C. EQE spectra (Figure 3b) indicate a broad range of photoresponse in 340–800 nm with an intensive peak at 550 nm accompanied by a relative weak shoulder in 630–710 nm. A second peak is found at 400 nm consistent with the UV-vis absorption spectra in Figure 3c. The BHJ films show reduced absorption after thermal treatment, but the absorption intensity reduction among 550–650 nm is slightly changed when annealing temperature rises. We further measured the reflectance of the active layers (Figure S8a). The increased reflectance in the 700 nm region is agreed with the increase in absorption intensity and reduction in EQE at the same wavelength position. As D/A

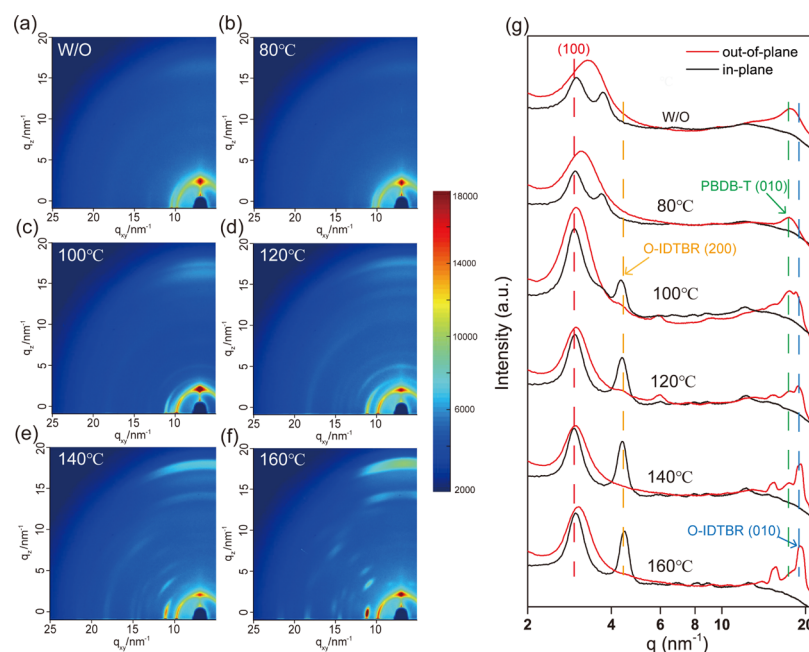


Figure 2. 2D GIWAXS patterns of the pristine BHJ film and the annealed BHJ films, respectively (a–f). (g) Corresponding integrated intensity information at in-plane and out-of-plane directions; green and blue dash lines are drawn to identify the PBDB-T and O-IDTBR (010) peaks.

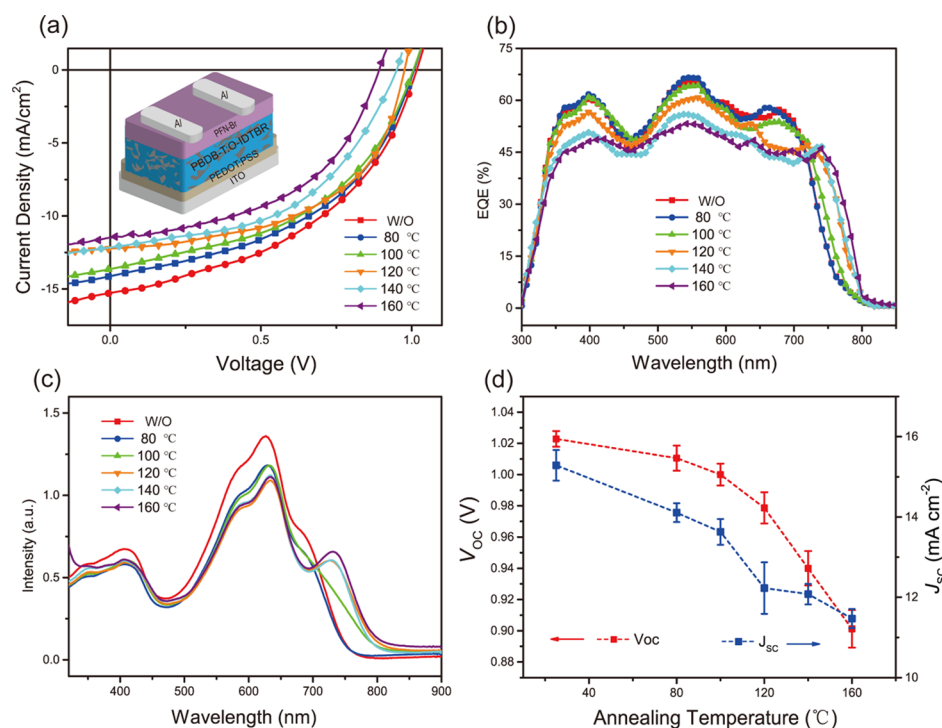


Figure 3. (a) J – V characteristics of PBDB-T:O-IDTBR OSC with active layers annealed at different temperatures. Inserted schematic is the structure of the OSC. (b) EQE spectra of corresponding OSC. (c) UV–vis absorption spectra of the PBDB-T:O-IDTBR pristine BHJ film and films annealed at 80, 100, 120, 140, and 160 °C. (d) V_{OC} and J_{SC} values as functions of annealing temperature (averaged over 10 devices).

crystallization intensity difference enlarge, the EQE decreased from 66.8 to 53.4%. The decrease in EQE is consistent well with the changes of absorption spectra, which is responsible for reduced J_{SC} . The emergence of the new absorption peak at 730 nm is the result of intensive π – π stacking induced intermolecular exciton absorption,²⁷ explaining the expansion of EQE spectra in 730–800 nm.

FF improvement has been proved a consequence of enhanced charge transport ability.^{28,29} The space-charge limited current (SCLC) method was used to examine the charge carrier mobilities. The charge mobility was acquired by fitting the J – V curves with the following equation³⁰

$$J = \frac{9}{8} \epsilon_0 \epsilon_r \mu_0 V^2 \exp(0.89 \sqrt{V/E_0 L}) / L^3 \quad (1)$$

Table 1. Photovoltaic Performances of PBDB-T:O-IDTBR BHJ Solar Cells with Active Layers Annealed at Different Temperatures Obtained Under AM 1.5 Illumination of 100 mW/cm^{2a}

annealing temperature [°C]	J_{sc} [mA cm ⁻²]	V_{oc} [V]	FF [%]	PCE [%]
W/O	15.2	1.02	48.7	7.5
100	13.6	1.00	54.3	7.4
80	14.2	1.01	53.1	7.6
120	12.2	0.98	55.2	6.6
140	12.1	0.94	55.3	6.3
160	11.5	0.90		5.7

^aThe results are averaged from more than 10 cells.

where J is the space charge-limited current density, ϵ_0 is the permittivity of vacuum, ϵ_r is the relative dielectric constant, $V = V_{appl} - V_{bi}$ is the difference between applied bias and built-in voltage, E_0 is the applied electric field, and L is the BHJ film thickness. The J - V curves and fitting results are shown in Figure S4. After annealing at 80 °C, the hole and electron mobilities were increased from 0.86×10^{-4} and 1.38×10^{-5} cm²/V s to 1.33×10^{-4} and 1.76×10^{-5} cm²/V s, respectively. The enhanced charge mobilities can be ascribed to the ordered molecular packing. Increased coherence length in BHJ films provides efficient carrier transport channel to support extension of the diffusion distance. These enhancements boost the FF of 48.7% in the pristine film to an improved 53.1% in the 80 °C annealed film.

3.4. Geminate and Nongeminate Recombination Mechanisms. Previous works have proven that the energy state distribution of conjugated materials is a complex structure rather than single-energy levels, as illustrated in Figure 4a.^{31,32}

Energetic disorder-related inhomogeneous broadening of HOMO or LUMO is a vital factor in geminate recombination processes and the demonstrated V_{oc} of bulk heterojunction OSCs.^{17,31} Gaussian distribution is suitable to describe the DOS under energetic disorder. The energy loss can be quantified by the width of the Gaussian DOS (defined as Δ_{HOMO} and Δ_{LUMO} for HOMO and LUMO, respectively) given by²¹

$$\Delta_{HOMO(LUMO)} = \sigma_{HOMO(LUMO)}^2 / k_B T \quad (2)$$

where σ is the parameter of energetic disorder, k_B is the Boltzmann constant, and T is Kelvin temperature. To quantify energetic disorder, temperature-correlated charge carrier mobilities were investigated in these differently crystallized BHJ films using the SCLC method. Figure 4b,c shows the charge mobilities under different temperatures among the films with multiple annealed temperatures. As the environment temperature increases, the charge carrier mobilities in all films get improved. This positive correlation indicates a distinct hopping transport dynamic. The relationship between disorder parameter σ and mobilities can be qualitatively illustrated by³³

$$\mu = \mu_{\infty} \exp\left(-\left(\frac{2\sigma}{3k_B T}\right)^2\right) \quad (3)$$

in which μ_{∞} represents the upper limit of mobilities when temperature approaches infinity. Fitting results of σ_{HOMO} and σ_{LUMO} are summarized in Table 2. It was found that the scale of energetic disorder is closely related to crystallinity. In all films, σ_{LUMO} is slightly larger than σ_{HOMO} about 4 meV, ascribing to larger hole mobilities. When the annealing temperature increases to 160 °C, the disorder scale shows a

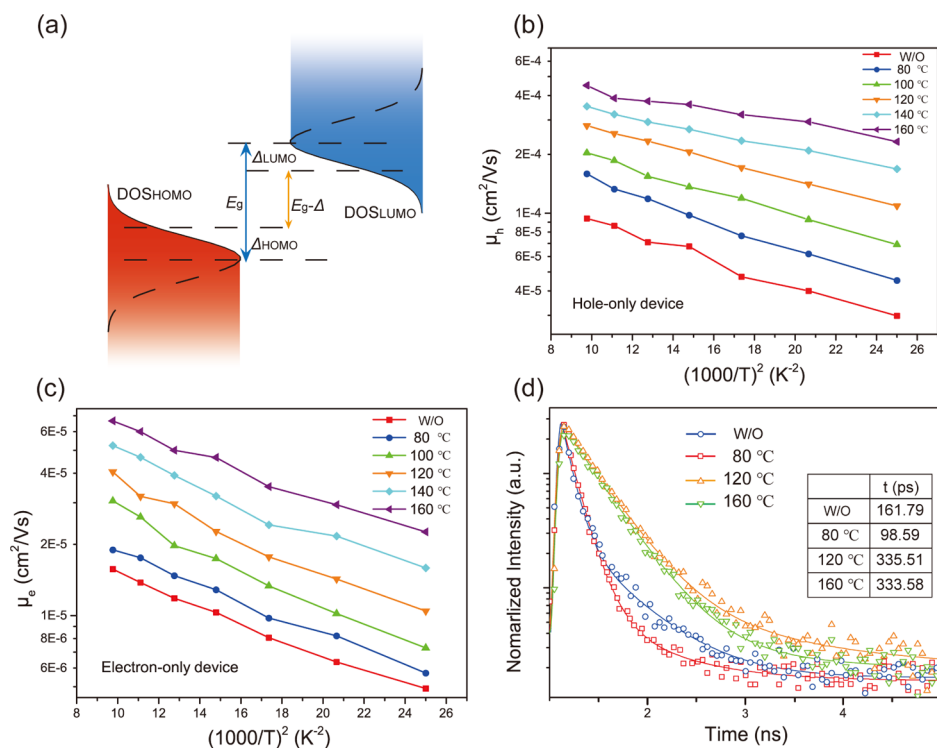


Figure 4. (a) Energy diagram of the D/A interface accounting the energetic disorder of HOMO and LUMO. Charge mobilities of (b) holes and (c) electrons in a variety of temperature-annealed BHJ films as the function of Kelvin temperature. (d) Fluorescence lifetime decay curves extracted in the selected spots in Figure S5a–d; the inset table summarizes the fitted lifetime.

Table 2. σ , Δ , and $\Delta V_{OC}^{non-rad}$ Values Determined from Temperature-Correlated Mobility Test and Integral Calculation

annealing temperature [°C]	σ_{HOMO} [meV]	σ_{LUMO} [meV]	Δ_{HOMO} [meV]	Δ_{LUMO} [meV]	Δ [meV]	V_{OC}^{rad} [V]	$\Delta V_{OC}^{non-rad}$ [V]
W/O	37	41	53	65	118	1.260	0.231
80	37	40	53	60	113	1.250	0.240
100	35	39	47	59	106	1.249	0.246
120	33	38	42	56	98	1.246	0.269
140	32	37	40	53	93	1.241	0.292
160	33	36	42	50	92	1.235	0.330

reducing trend, that is, the σ value of HOMO drops from 37 to 33 meV and that of LUMO reduces from 41 to 36 meV. We calculated the Gaussian distribution widths Δ_{HOMO} , Δ_{LUMO} , and their sum Δ (also showing in Table 2). The Δ value of the pristine film is ~ 118 meV, and it decreases continually to ~ 92 meV when the annealing temperature increases to 160 °C. The restricted energetics disorder can be attributed to the well-regulated molecular packing and increased CL. Restricted energetics disorder facilitates electrons and holes occupying a higher energy level and enlarging the energetics difference which results to an efficient exciton dissociation. Therefore, the crystallization-induced energetics disorder optimization weakens the interaction between electrons in LUMO and holes in HOMO, leading to impediment of geminate recombination.

Time-resolved fluorescence lifetime imaging microscopy (FLIM) can be adopted to visualize the detailed dynamics of the exciton and charge carriers in BHJ films.^{34,35} We employed FLIM to further verify the impeded geminate recombination. Figure S5 exhibits the scanning images and lifetime distribution histograms of the pristine film, films annealed at 80, 120, and 160 °C, respectively. Figure 4d shows the fluorescence decay dynamics of each film (corresponding points were marked in Figure S5a–d). The decay profiles are fitted with single-exponential decay function $I(t) = Ae^{-t/\tau}$. The detailed parameters were summarized in the inset table in Figure 4d. For the pristine PDBD-T:O-IDTBR film, the fitted result was 161.79 ps. A shortened lifetime of 98 ps was observed in the film annealed at 80 °C. However, the fluorescence lifetimes increased to 335 and 333 ps with the annealing temperature increasing to 120 and 160 °C. The increased fluorescence lifetime could be ascribed to rough morphology induced by excessive thermal annealing. As illustrated by AFM images in Figure S1, large and randomly distributed crystal grains occupy most scanning area in the films annealed at 120 and 160 °C. These grains not only impede efficient exciton dissociation induced by decreased D/A interface but also induce flaws in the blend films which might trap the singlet exciton and lead to extension of the fluorescence lifetime.³⁶ The film annealed at 80 °C maintains a smooth morphology which provides a sufficient D/A interface for charge transfer dynamics, as revealed by the minimum fluorescence lifetime, indicating a suppressed geminate recombination.

The nongeminate recombination occurred during charge transport can be investigated by nonradiative recombination V_{OC} loss ($\Delta V_{OC}^{non-rad}$). We calculated $\Delta V_{OC}^{non-rad}$ using the formula $\Delta V_{OC}^{non-rad} = V_{OC}^{rad} - V_{OC}$. V_{OC}^{rad} was given by eq 4³⁷

$$V_{OC}^{rad} = \frac{k_B T}{q} \ln \left(\frac{J_{SC}}{J_0} + 1 \right) \\ = \frac{k_B T}{q} \ln \left(\frac{q \int_0^\infty EQE(E) \cdot \phi_{AM1.5}(E) dE}{q \int_0^\infty EQE(E) \cdot \phi_{BB}(E, T) dE} + 1 \right) \quad (4)$$

where $\Phi_{AM1.5}$ represents the AM 1.5 solar radiation spectrum and Φ_{BB} is the blackbody spectrum at temperature T (300 K is used here). The determined value of V_{OC}^{rad} and $\Delta V_{OC}^{non-rad}$ is summarized in Table 2. Growing tendency of $\Delta V_{OC}^{non-rad}$ results in a difference of roughly 0.10 V between the upper and lower limit, 0.330 and 0.231 V for 160 °C annealed and pristine film, respectively. EL spectra were measured to investigate the energy level of CTS. In Figure S6, all normalized EL spectra show a single emission peak located in 848 nm, which indicates that the energy level of CTS is stable and barely affects energy loss among different crystallization conditions. Therefore, the enlargement in nonradiative voltage loss elucidates an increased probability of nongeminate recombination, which could be ascribed to the enlarged imbalance between electrons and hole mobilities induced by the variance in crystallinity of the donor and acceptor.²¹ As illustrated in GIWAXS results, the (010) peak at OOP direction shows no obvious superposition in the films annealed less than 100 °C, whose mobility ratios (calculated by μ_h/μ_e) are stabilized around 8 (Figure S7), and $\Delta V_{OC}^{non-rad}$ are changing in a restricted range from 0.23 to 0.25 V. When the film is annealed at 160 °C, O-IDTBR molecules exhibit more intensive crystallinity, which results in a mobility ratio beyond 10 as well as the largest $\Delta V_{OC}^{non-rad}$ of 0.330 V. IQE spectra (Figure S8b) of the OSCs are calculated based on the reflectance spectra (Figure S8a) using the following equation

$$IQE(\lambda) = \frac{EQE(\lambda)}{1 - R(\lambda)} \quad (5)$$

in which $R(\lambda)$ is the reflectance at certain wavelength. The IQE decrease with rising annealing temperature which exhibits a similar trend with EQE spectra. As proven above, thermal crystallization of D/A components suppresses geminate recombination, which can enhance the charge separation and in principle can improve the quantum efficiency. However, the enlarged nongeminate recombination energy loss impedes the charge collection and thus covers the separation improvement, leading to a decrease in quantum efficiency as well as the device performance. Therefore, the decreasing IQE is an evidence for the severe nongeminate recombination in films annealed at high temperature.

In order to illuminate the correlation between crystallinity and recombination energy loss dynamics, we defined D/A crystallization intensity ratio α calculated by $\alpha = P_{acceptor}/P_{donor}$ in which $P_{acceptor(donor)}$ represents the (010) and (020) peak area fraction of the acceptor (or donor) in GIWAXS OOP

signal integration curves. The change in α reveals a clear evolution of D/A crystallinity difference, that is, an initial decreased variance as α close to 1 and then increased variance as α far from 1 with the annealing temperature rising. The curves of the energetic disorder scale Δ and nonradiative recombination energy loss $\Delta V_{OC}^{non-rad}$ versus α were plotted separately in Figure 5. It can be directly distinguished that

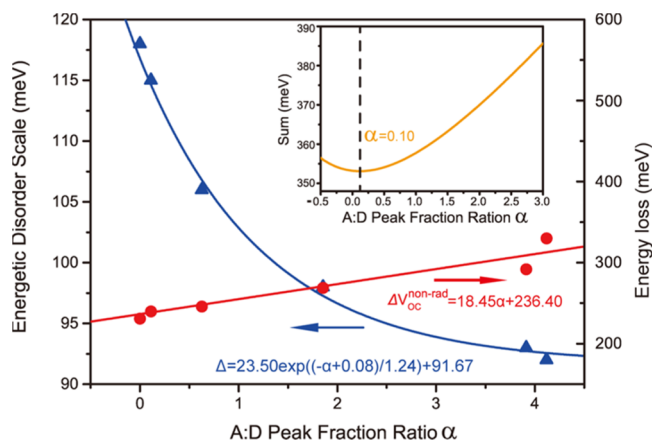


Figure 5. Data and fitting results of the energetic disorder scale Δ (blue) and nongeminate recombination loss $\Delta V_{OC}^{non-rad}$ (red) versus D/A crystallinity intensity ratio α . Inset plots the summation of the fitted formulas of Δ and $\Delta V_{OC}^{non-rad}$, in which the dash line marks the minimum energy loss ratio of $\alpha = 0.1$.

$\Delta V_{OC}^{non-rad}$ is linearly increasing as a function of α , while the relationship of Δ and α can be described with a perfect single-exponential decay function, confirmed by the fitting curve. The overall energy loss fitting result, as shown by the inset in Figure 5, indicates the existence of an α value of 0.10 that can obtain the minimum overall energy loss, which is almost identical with an α value of 0.11 obtained in the best performed OSCs annealed at 80 °C. These results elucidate that the most suitable D/A crystallinity does not mean same crystallinities. The 80 °C thermal treated film maintains a favorable morphology and endows rational crystallinity which restricted the broadening of energetic tail states. Meanwhile, the asymmetry of carrier mobility is not significant enough to induce a large nonradiative energy loss. However, the best ratio of D/A crystallization intensity might change in other non-fullerene-based solar cells, as small molecules exhibit quite different crystallinity, and the interaction with other components also strongly correlated with material properties.

4. CONCLUSIONS

In conclusion, we have characterized D/A crystallinity in a quantitative way and investigated crystallization-influenced geminate and nongeminate recombination mechanisms in the non-fullerene PBDB-T:O-IDTBR solar cells. Comparing to the pristine BHJ film, the crystallized films acquire a compact molecular packing mode and generate crystal domains in various sizes from a dozen to hundreds of nanometers. For the geminate recombination, intensive crystallinity can restrict the energetics disorder scale of HOMO and LUMO, which is favorable for charge transfer. Moderate phase separation induced by crystallization enhanced the charge transfer at the D/A interface that suppresses the geminate recombination as well. For the nongeminate recombination process occurred in charges transport, crystallinity difference of the donor and

acceptor results in charge mobilities imbalance and enlarged $\Delta V_{OC}^{non-rad}$, leading to intensive nongeminate recombination. The results reveal that crystallinity of donor and acceptor molecules closely affect the recombination energy loss. Based on the quantitative analysis of GIWAXS signals, we found that the rational crystallization intensity ratio between D/A components is the key factor of achieving minimum energy loss, that is, finding the balance point between the decrease of geminate recombination and the enlargement of nongeminate. Further issues still need to be settled, for instance, the correlation between crystallinity and energy losses mechanisms in ternary systems and precise experimental methods to manipulate components crystallization dynamics.

■ ASSOCIATED CONTENT

Supporting Information

The Supporting Information is available free of charge on the ACS Publications website at DOI: 10.1021/acs.jpcc.9b03572.

AFM height images of pristine and annealed films; GIWAXS patterns and integrated signals of neat PBDB-T and O-IDTBR films; results of multipeak fitting of the OOP (010) peaks in annealed films; results of room temperature $J-V$ characteristics; FLIM scanned images and lifetime distributions; EL spectrum collected from corresponding OSCs; the change in the mobility ratio (hole to electron) of annealed devices; reflectance spectra and calculated IQE spectra; and details for GIWAXS peak analysis (PDF)

■ AUTHOR INFORMATION

Corresponding Author

*E-mail: haoxt@sdu.edu.cn.

ORCID

Xiao-Tao Hao: 0000-0002-0197-6545

Notes

The authors declare no competing financial interest.

■ ACKNOWLEDGMENTS

This work was supported by the National Natural Science Foundation of China (11774204) and the Key R & D Programs of Shandong Province, China (2018GGX103004). Support from the ARC Centre of Excellence in Exciton Science (CE170100026) is acknowledged. The authors would like to thank the Shanghai Synchrotron Radiation Facility (beam line BL16B1) for providing the beam time for GIXS measurements.

■ REFERENCES

- (1) Yuan, J.; Zhang, Y.; Zhou, L.; Zhang, G.; Yip, H.-L.; Lau, T.-K.; Lu, X.; Zhu, C.; Peng, H.; Johnson, P. A.; et al. Single-Junction Organic Solar Cell with over 15% Efficiency Using Fused-Ring Acceptor with Electron-Deficient Core. *Joule* **2019**, 3, 1140.
- (2) Lin, H.; Chen, S.; Li, Z.; Lai, J. Y. L.; Yang, G.; McAfee, T.; Jiang, K.; Li, Y.; Liu, Y.; Hu, H.; et al. High-Performance Non-Fullerene Polymer Solar Cells Based on a Pair of Donor-Acceptor Materials with Complementary Absorption Properties. *Adv. Mater.* **2015**, 27, 7299–7304.
- (3) Xiao, B.; Tang, A.; Zhang, J.; Mahmood, A.; Wei, Z.; Zhou, E. Achievement of High Voc of 1.02 V for P3ht-Based Organic Solar Cell Using a Benzotriazole-Containing Non-Fullerene Acceptor. *Adv. Energy Mater.* **2017**, 7, 1602269.
- (4) Lin, Y.; Cheng, P.; Li, Y.; Zhan, X. A 3d Star-Shaped Non-Fullerene Acceptor for Solution-Processed Organic Solar Cells with a

High Open-Circuit Voltage of 1.18 V. *Chem. Commun.* **2012**, 48, 4773–4775.

(5) Holliday, S.; Ashraf, R. S.; Wadsworth, A.; Baran, D.; Yousaf, S. A.; Nielsen, C. B.; Tan, C. H.; Dimitrov, S. D.; Shang, Z.; Gasparini, N.; et al. High-Efficiency and Air-Stable P3ht-Based Polymer Solar Cells with a New Non-Fullerene Acceptor. *Nat. Commun.* **2016**, 7, 11585.

(6) Li, S.; Ye, L.; Zhao, W.; Zhang, S.; Mukherjee, S.; Ade, H.; Hou, J. Energy-Level Modulation of Small-Molecule Electron Acceptors to Achieve over 12% Efficiency in Polymer Solar Cells. *Adv. Mater.* **2016**, 28, 9423–9429.

(7) Chao, P.; Mu, Z.; Wang, H.; Mo, D.; Chen, H.; Meng, H.; Chen, W.; He, F. Chlorination of Side Chains: A Strategy for Achieving a High Open Circuit Voltage over 1.0 V in Benzo[1,2-B:4,5-B']Dithiophene-Based Non-Fullerene Solar Cells. *ACS Appl. Energy Mater.* **2018**, 1, 2365–2372.

(8) Li, S.; Liu, W.; Shi, M.; Mai, J.; Lau, T.-K.; Wan, J.; Lu, X.; Li, C.-Z.; Chen, H. A Spirofluorene and Diketopyrrolopyrrole Moieties Based Non-Fullerene Acceptor for Efficient and Thermally Stable Polymer Solar Cells with High Open-Circuit Voltage. *Energy Environ. Sci.* **2016**, 9, 604–610.

(9) Zhao, J.; Li, Y.; Lin, H.; Liu, Y.; Jiang, K.; Mu, C.; Ma, T.; Lin Lai, J. Y.; Hu, H.; Yu, D.; et al. High-Efficiency Non-Fullerene Organic Solar Cells Enabled by a Difluorobenzothiadiazole-Based Donor Polymer Combined with a Properly Matched Small Molecule Acceptor. *Energy Environ. Sci.* **2015**, 8, 520–525.

(10) Baran, D.; Kirchartz, T.; Wheeler, S.; Dimitrov, S.; Abdelsamie, M.; Gorman, J.; Ashraf, R. S.; Holliday, S.; Wadsworth, A.; Gasparini, N.; et al. Reduced Voltage Losses Yield 10% Efficient Fullerene Free Organic Solar Cells with >1 V Open Circuit Voltages. *Energy Environ. Sci.* **2016**, 9, 3783–3793.

(11) Burke, T. M.; Sweetnam, S.; Vandewal, K.; McGehee, M. D. Beyond Langevin Recombination: How Equilibrium between Free Carriers and Charge Transfer States Determines the Open-Circuit Voltage of Organic Solar Cells. *Adv. Energy Mater.* **2015**, 5, 1500123.

(12) Chen, X.-K.; Ravva, M. K.; Li, H.; Ryno, S. M.; Brédas, J.-L. Effect of Molecular Packing and Charge Delocalization on the Nonradiative Recombination of Charge-Transfer States in Organic Solar Cells. *Adv. Energy Mater.* **2016**, 6, 1601325.

(13) Tang, Z.; Wang, J.; Melianas, A.; Wu, Y.; Kroon, R.; Li, W.; Ma, W.; Andersson, M. R.; Ma, Z.; Cai, W.; et al. Relating Open-Circuit Voltage Losses to the Active Layer Morphology and Contact Selectivity in Organic Solar Cells. *J. Mater. Chem. A* **2018**, 6, 12574–12581.

(14) Vandewal, K.; Albrecht, S.; Hoke, E. T.; Graham, K. R.; Widmer, J.; Douglas, J. D.; Schubert, M.; Mateker, W. R.; Bloking, J. T.; Burkhard, G. F.; et al. Efficient Charge Generation by Relaxed Charge-Transfer States at Organic Interfaces. *Nat. Mater.* **2014**, 13, 63–68.

(15) Vandewal, K.; Tvingstedt, K.; Gadisa, A.; Inganäs, O.; Manca, J. V. Relating the Open-Circuit Voltage to Interface Molecular Properties of Donor:Acceptor Bulk Heterojunction Solar Cells. *Phys. Rev. B: Condens. Matter Mater. Phys.* **2010**, 81, 125204.

(16) Benduhn, J.; Tvingstedt, K.; Piersimoni, F.; Ullbrich, S.; Fan, Y.; Tropiano, M.; McGarry, K. A.; Zeika, O.; Riede, M. K.; Douglas, C. J.; et al. Intrinsic Non-Radiative Voltage Losses in Fullerene-Based Organic Solar Cells. *Nat. Energy* **2017**, 2, 17053.

(17) Blakesley, J. C.; Neher, D. Relationship between Energetic Disorder and Open-Circuit Voltage in Bulk Heterojunction Organic Solar Cells. *Phys. Rev. B: Condens. Matter Mater. Phys.* **2011**, 84, 075210.

(18) Gao, F.; Tress, W.; Wang, J.; Inganäs, O. Temperature Dependence of Charge Carrier Generation in Organic Photovoltaics. *Phys. Rev. Lett.* **2015**, 114, 128701.

(19) Yang, D.; Wang, Y.; Sano, T.; Gao, F.; Sasabe, H.; Kido, J. A Minimal Non-Radiative Recombination Loss for Efficient Non-Fullerene All-Small-Molecule Organic Solar Cells with a Low Energy Loss of 0.54 eV and High Open-Circuit Voltage of 1.15 V. *J. Mater. Chem. A* **2018**, 6, 13918–13924.

(20) Wang, Y.; Wu, B.; Wu, Z.; Lan, Z.; Li, Y.; Zhang, M.; Zhu, F. Origin of Efficient Inverted Nonfullerene Organic Solar Cells: Enhancement of Charge Extraction and Suppression of Bimolecular Recombination Enabled by Augmented Internal Electric Field. *J. Phys. Chem. Lett.* **2017**, 8, 5264–5271.

(21) Xie, S.; Xia, Y.; Zheng, Z.; Zhang, X.; Yuan, J.; Zhou, H.; Zhang, Y. Effects of Nonradiative Losses at Charge Transfer States and Energetic Disorder on the Open-Circuit Voltage in Nonfullerene Organic Solar Cells. *Adv. Funct. Mater.* **2018**, 28, 1705659.

(22) Gao, F.; Himmelberger, S.; Andersson, M.; Hanifi, D.; Xia, Y.; Zhang, S.; Wang, J.; Hou, J.; Salteo, A.; Inganäs, O. The Effect of Processing Additives on Energetic Disorder in Highly Efficient Organic Photovoltaics: A Case Study on Pbdttt-C-T:PC71 Bm. *Adv. Mater.* **2015**, 27, 3868–3873.

(23) Heumueller, T.; Burke, T. M.; Mateker, W. R.; Sachs-Quintana, I. T.; Vandewal, K.; Brabec, C. J.; McGehee, M. D. Disorder-Induced Open-Circuit Voltage Losses in Organic Solar Cells During Photoinduced Burn-In. *Adv. Energy Mater.* **2015**, 5, 1500111.

(24) Zhao, W.; Qian, D.; Zhang, S.; Li, S.; Inganäs, O.; Gao, F.; Hou, J. Fullerene-Free Polymer Solar Cells with over 11% Efficiency and Excellent Thermal Stability. *Adv. Mater.* **2016**, 28, 4734–4739.

(25) Qian, D.; Zheng, Z.; Yao, H.; Tress, W.; Hopper, T. R.; Chen, S.; Li, S.; Liu, J.; Chen, S.; Zhang, J.; et al. Design Rules for Minimizing Voltage Losses in High-Efficiency Organic Solar Cells. *Nat. Mater.* **2018**, 17, 703–709.

(26) Patterson, A. L. The Scherrer Formula for X-Ray Particle Size Determination. *Phys. Rev.* **1939**, 56, 978–982.

(27) James, D. T.; Frost, J. M.; Wade, J.; Nelson, J.; Kim, J.-S. Controlling Microstructure of Pentacene Derivatives by Solution Processing: Impact of Structural Anisotropy on Optoelectronic Properties. *ACS Nano* **2013**, 7, 7983–7991.

(28) Proctor, C. M.; Love, J. A.; Nguyen, T.-Q. Mobility Guidelines for High Fill Factor Solution-Processed Small Molecule Solar Cells. *Adv. Mater.* **2014**, 26, 5957–5961.

(29) Bartelt, J. A.; Lam, D.; Burke, T. M.; Sweetnam, S. M.; McGehee, M. D. Charge-Carrier Mobility Requirements for Bulk Heterojunction Solar Cells with High Fill Factor and External Quantum Efficiency >90%. *Adv. Energy Mater.* **2015**, 5, 1500577.

(30) Malliaras, G. G.; Salem, J. R.; Brock, P. J.; Scott, C. Electrical Characteristics and Efficiency of Single-Layer Organic Light-Emitting Diodes. *Phys. Rev. B: Condens. Matter Mater. Phys.* **1998**, 58, R13411.

(31) Garcia-Belmonte, G.; Bisquert, J. Open-Circuit Voltage Limit Caused by Recombination through Tail States in Bulk Heterojunction Polymer-Fullerene Solar Cells. *Appl. Phys. Lett.* **2010**, 96, 113301.

(32) Blakesley, J. C.; Greenham, N. C. Charge Transfer at Polymer-Electrode Interfaces: The Effect of Energetic Disorder and Thermal Injection on Band Bending and Open-Circuit Voltage. *J. Appl. Phys.* **2009**, 106, 034507.

(33) Miller, A.; Abrahams, E. Impurity Conduction at Low Concentrations. *Phys. Rev.* **1960**, 120, 745–755.

(34) Hao, X.-T.; McKimmie, L. J.; Smith, T. A. Spatial Fluorescence Inhomogeneities in Light-Emitting Conjugated Polymer Films. *J. Phys. Chem. Lett.* **2011**, 2, 1520–1525.

(35) Bi, P.; Xiao, T.; Yang, X.; Niu, M.; Wen, Z.; Zhang, K.; Qin, W.; So, S. K.; Lu, G.; Hao, X.; et al. Regulating the Vertical Phase Distribution by Fullerene-Derivative in High Performance Ternary Organic Solar Cells. *Nano Energy* **2018**, 46, 81–90.

(36) Bi, P.; Zheng, F.; Yang, X.; Niu, M.; Feng, L.; Qin, W.; Hao, X. Dual Förster Resonance Energy Transfer Effects in Non-Fullerene Ternary Organic Solar Cells with the Third Component Embedded in the Donor and Acceptor. *J. Mater. Chem. A* **2017**, 5, 12120–12130.

(37) Ndjawa, G. O. N.; Graham, K. R.; Mollinger, S.; Wu, D. M.; Hanifi, D.; Prasanna, R.; Rose, B. D.; Dey, S.; Yu, L.; Brédas, J.-L.; et al. Open-Circuit Voltage in Organic Solar Cells: The Impacts of Donor Semicrystallinity and Coexistence of Multiple Interfacial Charge-Transfer Bands. *Adv. Funct. Mater.* **2017**, 7, 1601995.